

# A Symmetry-Enabled Direct Quantum Protocol for Many-Body Green's Functions

Changhao Yi<sup>1</sup> and Cunlu Zhou<sup>2,3</sup>

<sup>1</sup>*Department of Physics, Shanghai University, Shanghai, China*

<sup>2</sup>*Department of Computer Science, Université de Sherbrooke, QC, Canada*

<sup>3</sup>*Institut quantique, Université de Sherbrooke, QC, Canada*

(Dated: March 3, 2026)

We present a symmetry-enabled direct quantum protocol for computing many-body Green's functions, a central tool for studying strongly correlated quantum systems. Our protocol relies only on native time evolution and straightforward measurements available on current hardware platforms. By exploiting parity symmetry—satisfied by a broad class of Hamiltonians in condensed matter physics and quantum chemistry, including the Fermi–Hubbard and Heisenberg models—we introduce a tailored quench spectroscopy scheme that recovers both the real and imaginary parts of two-point time correlators, from which Green's functions can be reconstructed via efficient classical signal processing. We further develop a tailored symmetric quantum Gibbs sampler that prepares parity-resolved (symmetric and antisymmetric) thermal states, enabling finite-temperature extensions within the same framework. Finally, we show that the same symmetry-based measurement primitive extends naturally to out-of-time-ordered correlators (OTOCs). Our results provide a practical route to estimating symmetry-resolved dynamical correlators on near-term and early fault-tolerant quantum hardware.

## I. INTRODUCTION

Many-body Green's functions are essential tools for probing strongly interacting many-body systems [1]. They compactly describe the propagation of particles and excitations without explicit wave-function representations, and they encode key information about the density of states and band structure, which underpin phenomena such as superconductivity, magnetism, and phase transitions. Experimentally, spectroscopic techniques can be used to extract Green's-function information: for example, angle-resolved photoemission spectroscopy (ARPES) [2] measures the momentum-resolved spectral function associated with single-particle Green's functions, while resonant inelastic X-ray scattering (RIXS) [3] probes collective excitations encoded in higher-order correlation functions. On the computational side, classical approaches face severe limitations when calculating these dynamical quantities. For example, exact diagonalization [4] is restricted to small clusters due to the exponential growth of the Hilbert space. While Quantum Monte Carlo methods [5] scale better for static properties, they struggle with the dynamical sign problem and the ill-conditioned analytic continuation required to extract real-time Green's functions from imaginary time. Similarly, tensor network states [6], though powerful in 1D, are limited by the rapid growth of entanglement entropy during non-equilibrium time evolution, which requires an exponentially growing bond dimension to maintain accuracy.

At a fundamental level, Green's functions are time-ordered correlation functions. Quantum computing offers a promising route to access them by enabling coherent real-time evolution and the measurement of dynamical correlators, potentially bypassing several bottlenecks faced by classical simulations. Many prominent quantum algorithms has been proposed, such as methods based

on phase estimation [7–12] and variational approaches [13–15]. However, such methods often rely on ancilla-assisted interference circuits and controlled time evolution to extract complex-valued correlators, which can be prohibitively resource-intensive on near-term hardware. In particular, controlled implementations of large unitaries substantially increase circuit depth and error rates, while also placing stringent demands on gate fidelity and coherence. These challenges are especially acute for current noisy intermediate-scale quantum (NISQ) devices [16], and remain nontrivial even in the early fault-tolerant regime [17].

To circumvent these overheads, a complementary class of quantum algorithms has recently gained traction by avoiding controlled unitaries and, in many cases, ancilla qubits. For instance, *quench spectroscopy* (QS) [9, 11, 18–20], a widely used protocol inspired by Ramsey interferometry, can be used to probe dynamical response functions. However, early studies such as [20] focused on fermionic correlation functions under translation symmetry, which restricts the accessible information to the imaginary part of time correlators. Closely related, the *linear-response framework* (LRF) [21–23] exploits the connection between Green's functions and response theory by introducing a weak time-dependent perturbation,  $H(t) = H + \varepsilon A(t)$ , and extracting correlators from the leading-order contribution to measured expectation values such as  $\langle A(t) \rangle$ . While conceptually simple, this approach typically requires simulating time-dependent Hamiltonians, and the recovered correlators are generally approximate due to higher-order corrections (except in [23]). Another route is *quantum imaginary time evolution* (QITE) [24–26], which implements normalized imaginary-time evolution (e.g., via Trotter–Suzuki decompositions) and introduces an imaginary-time shift  $t \rightarrow t + i\tau$ . Multi-time correlators can then be obtained from derivatives with respect to  $\tau$ , but the

accuracy is controlled by the asymptotic limit  $\tau \rightarrow 0$ . The *direct Krylov space* (DKS) method [27, 28] instead computes Green's functions recursively using analytically derived coefficients estimated from states, observables, and the Hamiltonian, thereby avoiding explicit quantum dynamics. However, this advantage comes at the cost of a high sample complexity that grows with the problem size. Moreover, subspace methods such as DKS can be sensitive to noise and estimation errors, particularly as the recursion depth increases [28, 29]. Finally, the *direct measurement* scheme [30] leverages mid-circuit measurements (MCMs) to access the real part of time correlators without assumptions on the initial state. Despite its generality and simplicity, MCM-based protocols remain challenging on current hardware due to slow and noisy MCMs and crosstalk that can disturb nearby qubits.

In this work, we introduce an ancilla-free and noise-resilient direct quantum protocol for estimating both the real and imaginary parts of two-point time correlators by exploiting *parity symmetry* [1], from which Green's functions can be reconstructed via efficient classical signal analysis. We refer to this approach as *tailored quench spectroscopy* (TQS). Specifically, we consider Hamiltonians that commute with a parity operator  $P$ , while the observables of interest  $A$  and  $B$  anti-commute with  $P$ . This condition is satisfied by a broad class of models central to condensed matter physics and quantum chemistry, including the Fermi-Hubbard and Heisenberg models. An overview of the protocol is provided in Fig. 1.

By designing tailored quench operators, we extend the standard QS method [20] to access bosonic correlation functions, enabling direct evaluation of the real part of time correlators. Compared to other ancilla-free protocols, such as LRF and QITE, our TQS approach offers several advantages: i) it requires only time-independent Hamiltonian evolution, thereby avoiding the simulation of time-dependent dynamics and reducing experimental complexity; ii) it enables exact, non-perturbative recovery of correlators, substantially mitigating systematic errors; and iii) unlike imaginary-time methods, which perturb the state via  $e^{-\tau O}$  and typically require additional overhead (e.g., Trotterization or dissipative evolution), it relies on considerably simpler operations.

In developing TQS protocols for finite-temperature Green's functions, we also introduce a tailored *symmetric quantum Gibbs sampler* for preparing symmetric and antisymmetric thermal states, which may be of independent interest.

The remainder of the paper is organized as follows. In Sec. II, we review the relationship between two-point time correlators and many-body Green's functions, parity symmetry, and the quench spectroscopy approach. In Sec. III, we present the symmetry-enabled TQS protocol in detail. We generalize the method to out-of-time-ordered correlators (OTOCs) in Sec. III C. Complexity and error analyses are provided in Sec. IV, and numerical simulations are reported in Sec. V. We conclude in Sec. VI with a discussion of future directions.

## II. BACKGROUND

### A. Many-body Green's functions and two-point time correlators

We begin by clarifying the relationship between two-point time correlators and the Lehmann representation of many-body Green's functions. Consider a Hamiltonian  $H$  with spectral decomposition  $H = \sum_{n=0}^{d-1} E_n |n\rangle\langle n|$ , and let  $O_a$  and  $O_b$  be two operators. In many-body physics, the two-point correlator is

$$C(O_a, O_b, t_1, t_2) := \text{Tr}[\rho O_a(t_1) O_b(t_2)], \quad (1)$$

where  $O(t) := e^{iHt} O e^{-iHt}$ . If the initial state is stationary with respect to  $H$  (e.g., a Gibbs state  $\rho_\beta = e^{-\beta H} / \text{Tr}(e^{-\beta H})$ , so that  $[\rho, H] = 0$ ), then the correlator depends only on the time difference and can be written as

$$C(O_a, O_b, t) = \text{Tr}[\rho O_a O_b(t)]. \quad (2)$$

Using the spectral decomposition of  $H$ , we obtain the expansion

$$C(O_a, O_b, t) = \sum_{m,n} \langle n|O_b|m\rangle \langle m|\rho O_a|n\rangle e^{i(E_m - E_n)t}. \quad (3)$$

We define the Green's function by a one-sided Fourier (Laplace) transform,

$$G(z) = \int_0^\infty dt e^{izt} C(O_a, O_b, -t), \quad \text{Im } z > 0, \quad (4)$$

which yields the Lehmann representation [31]

$$G(z) = \sum_{m,n} \frac{\langle n|O_b|m\rangle \langle m|\rho O_a|n\rangle}{z - (E_m - E_n)}, \quad \text{Im } z > 0. \quad (5)$$

Green's functions are commonly expressed either in the time domain, through the correlator  $C$ , or in the frequency domain, through Eq. (5); in this work we focus on the Lehmann representation. See Appendix A1 for additional background.

In fermionic systems,  $O_a$  and  $O_b$  are typically linear combinations of fermionic annihilation and creation operators  $\{c_i, c_i^\dagger\}_i$ . For example, if  $O_a = \sum_i a_i c_i$  and  $O_b = \sum_{i'} b_{i'} c_{i'}^\dagger$ , then by linearity

$$C(O_a, O_b, t) = \sum_{i,i'} a_i b_{i'} C(c_i, c_{i'}^\dagger, t). \quad (6)$$

Thus, it suffices to estimate correlators of the form  $C(c_i, c_{i'}^\dagger, t)$ . Under the Jordan-Wigner transformation (see Appendix A2), each fermionic operator can be written as a linear combination of two Pauli strings (equivalently, Majorana operators), i.e.,  $c_i = A + iB$  with Pauli operators  $A$  and  $B$  that anticommute. Writing  $c_i = A_0 + iB_0$  and  $c_{i'} = A_1 + iB_1$ , we obtain

$$C(c_i, c_{i'}^\dagger, t) = C(A_0, A_1, t) + C(B_0, B_1, t) - iC(A_0, B_1, t) + iC(B_0, A_1, t). \quad (7)$$

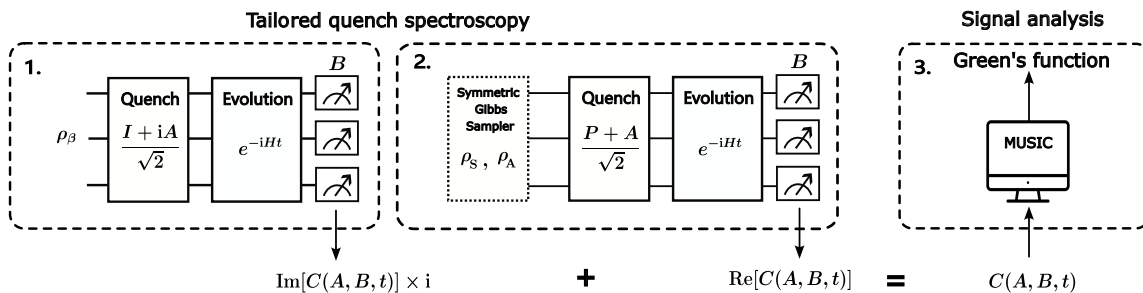


FIG. 1. Direct quantum protocol for computing many-body Green's functions via tailored quench spectroscopy. For an initial thermal state  $\rho_\beta$  (with  $\beta \rightarrow \infty$  corresponding to the zero-temperature limit, so that the thermal state becomes the ground state), the imaginary and real parts of the two-point time correlator  $C(A, B, t)$  are obtained by applying the tailored quench operators  $(I + iA)/\sqrt{2}$  and  $(P + A)/\sqrt{2}$ , respectively, followed by time evolution under  $e^{-iHt}$  and measurements in the eigenbasis of the observable  $B$ . For a thermal initial state, the symmetric and antisymmetric thermal states  $\rho_S$  and  $\rho_A$  are prepared using a tailored symmetric quantum Gibbs sampler (step 2). For a ground-state initial condition, this thermal-state preparation step is not needed. The full Green's function is then reconstructed via classical signal-processing routines (e.g., MULTIPLE SIGNAL Classification (MUSIC)).

Consequently, the problem reduces to estimating general two-point correlators of the form  $C(A, B, t)$ , which will be the primary focus of the following sections.

## B. Parity symmetry

If there exists an operator  $P$  that is unitary and Hermitian and satisfies  $[H, P] = 0$ , then we say that  $H$  has a parity symmetry and refer to  $P$  as a parity operator. This condition is common in many lattice models. For example, the Heisenberg (XXZ) chain

$$H_{\text{XXZ}} = J_X \left( \sum_{n=0}^{N-2} X_n X_{n+1} + Y_n Y_{n+1} \right) + J_Z \sum_{n=0}^{N-2} Z_n Z_{n+1} + h \sum_{n=0}^{N-1} Z_n. \quad (8)$$

commutes with the global  $\mathbb{Z}_2$  parity operator  $P := \prod_{j=0}^{N-1} Z_j$ .

As another example, consider the spinful Fermi-Hubbard model

$$H_{\text{FH}} = - \sum_{j=0}^{N-1} \sum_{\sigma=\uparrow, \downarrow} \left( c_{j,\sigma}^\dagger c_{j+1,\sigma} + c_{j+1,\sigma}^\dagger c_{j,\sigma} \right) + h_U \sum_{j=0}^{N-1} n_{j,\uparrow} n_{j,\downarrow}. \quad (9)$$

A natural parity symmetry here is fermion-number parity,

$$P := (-1)^{\hat{N}} = \prod_{j,\sigma} e^{i\pi n_{j,\sigma}}, \quad \hat{N} := \sum_{j,\sigma} n_{j,\sigma}. \quad (10)$$

Under the Jordan-Wigner transformation, this maps to

the Pauli-Z string over all spin-orbitals (qubits),

$$P = \prod_{q=0}^{2N-1} Z_q. \quad (11)$$

Throughout the remainder of the paper, we choose  $\{|n\rangle\}_{n=0}^{d-1}$  to be a common eigenbasis of  $H$  and  $P$ , so that

$$H|n\rangle = E_n|n\rangle, \quad P|n\rangle = p_n|n\rangle, \quad p_n \in \{\pm 1\}. \quad (12)$$

We say that  $|n\rangle$  has even parity if  $p_n = +1$  and odd parity if  $p_n = -1$ . Let  $\mathcal{H}_{\text{even}}$  and  $\mathcal{H}_{\text{odd}}$  denote the corresponding parity sectors (subspaces). We also define the parity projectors

$$\Pi_S := \frac{I + P}{2}, \quad \Pi_A := \frac{I - P}{2}, \quad (13)$$

which form a two-outcome parity POVM. Here  $I$  denotes the identity operator.

We will use the following selection rule (see Appendix B 1 for a proof).

**Lemma 1.** *Suppose  $[H, P] = 0$  and  $\{A, P\} = 0$ , and let  $|m\rangle, |n\rangle$  be eigenstates of  $H$  (and hence of  $P$ ). If  $\langle n|A|m\rangle \neq 0$ , then  $|m\rangle$  and  $|n\rangle$  have opposite parity, i.e.,  $p_m p_n = -1$ .*

## C. Quench spectroscopy

Quench spectroscopy (QS) is a simple yet powerful technique for probing dynamical properties of quantum systems. The central idea is to apply a sudden perturbation to a prepared state and then monitor the ensuing unitary dynamics under a time-independent Hamiltonian. By measuring suitable observables as a function of time, one obtains a signal whose oscillation frequencies correspond to energy differences in the spec-

trum. Classical post-processing of this time-domain signal then yields spectral information and dynamical correlation functions, without requiring controlled time evolution or other time-dependent operations.

Building on the QS method in Refs. [20, 32], one can directly access the *imaginary part* of a two-point time correlator under minimal assumptions: the initial state may be either equilibrium or nonequilibrium. To formalize the protocol, we define the *quench function* as the expectation value of a measurement outcome,

$$Q_{\rho,M}(U) := \text{Tr}(U\rho U^\dagger M), \quad (14)$$

where  $U$  denotes the unitary implemented in the QS experiment and  $M$  is the measured observable. Assuming  $A$  is a Hermitian operator satisfying  $A^2 = I$ , and applying the quench operator

$$U_{\text{Im}} := e^{i\pi A/4} = \frac{I + iA}{\sqrt{2}}, \quad (15)$$

one obtains

$$\begin{aligned} \text{Im}[C(A, B, t)] &= Q_{\rho,B}(e^{-iHt}U_{\text{Im}}) \\ &\quad - \frac{1}{2}Q_{\rho,B}(e^{-iHt}A) - \frac{1}{2}Q_{\rho,B}(e^{-iHt}). \end{aligned} \quad (16)$$

All terms on the right-hand side can be measured directly on a quantum device, making QS a practical route to extracting imaginary time-correlator information, equivalently fermionic response functions of the form  $iC(A, B, t) - iC(B, A, t)$ . The nontrivial step is to access the *real part* of time correlators, or equivalently bosonic response functions of the form  $C(A, B, t) + C(B, A, t)$ . In the following sections, we show how to achieve this by introducing a *tailored quench operator* and exploiting symmetries inherent to the system.

### III. SYMMETRY-ENABLED PROTOCOLS FOR TIME CORRELATORS

From now on, we focus on systems with a  $\mathbb{Z}_2$  (parity) symmetry. Concretely, we assume there exists a parity operator  $P$  such that

$$[P, H] = 0, \quad P^\dagger = P, \quad P^2 = I. \quad (17)$$

We consider Hermitian observables  $A$  and  $B$  satisfying

$$A^2 = I, \quad \{A, P\} = \{B, P\} = 0, \quad (18)$$

and we assume the initial state is parity-symmetric,

$$[\rho, P] = 0. \quad (19)$$

Prominent examples include equilibrium (Gibbs) states  $\rho_\beta = e^{-\beta H} / \text{Tr}(e^{-\beta H})$ , and the ground state recovered in the limit  $\beta \rightarrow \infty$ .

#### A. Tailored quench spectroscopy

To access the real part of a two-point time correlator, we introduce the quench operator

$$U_{\text{Re}} := \frac{P + A}{\sqrt{2}}. \quad (20)$$

Since  $\{P, A\} = 0$  and  $P^2 = A^2 = I$ , the operator  $PA$  satisfies  $(PA)^\dagger = -PA$  and  $(PA)^2 = -I$ , so  $G := -iPA$  is Hermitian and obeys  $G^2 = I$ . Consequently,  $U_{\text{Re}}$  admits the decomposition

$$\frac{P + A}{\sqrt{2}} = P \exp\left(i\frac{\pi}{4}G\right) = P \exp\left[i\frac{\pi}{4}(-iPA)\right]. \quad (21)$$

In particular, when  $P$  and  $A$  are Pauli strings,  $G$  is also a Pauli string and the implementation reduces to a single Pauli rotation (with Bloch-sphere rotation angle  $\pi/2$ ).

We refer to the protocol based on the two quench operators  $U_{\text{Im}}$  and  $U_{\text{Re}}$  as *tailored quench spectroscopy* (TQS). For an  $N$ -qubit system, both operators can be implemented with circuit depth  $\mathcal{O}(\log N)$  using only CNOTs and single-qubit gates [33].

With the quench operator  $U_{\text{Re}}$ , one obtains

$$\begin{aligned} \text{Re}[C(PA, B, t)] &= Q_{\rho,B}(e^{-iHt}U_{\text{Re}}) \\ &\quad - \frac{1}{2}Q_{\rho,B}(e^{-iHt}P) - \frac{1}{2}Q_{\rho,B}(e^{-iHt}A). \end{aligned} \quad (22)$$

Importantly, if the initial state  $\rho$  has a well-defined parity, i.e.,  $P\rho = p\rho$  with  $p \in \{+1, -1\}$ , then  $C(PA, B, t) = pC(A, B, t)$ . Consequently, the left-hand side of Eq. (22) directly yields  $\text{Re}[C(A, B, t)]$  up to the known sign  $p$ , which can be fixed from the parity sector of the initial state. Together with the QS identity for  $\text{Im}[C(A, B, t)]$ , the full complex correlator can therefore be reconstructed from a linear combination of six experimentally accessible quench functions.

Moreover, when  $\{B, P\} = 0$ , several terms in Eq. (16) and Eq. (22) vanish identically by symmetry. As a result, the full complex correlator can be reconstructed using only two quench functions. This simplification is summarized in the following theorem; see Appendix B 2 for the proof.

**Theorem 1.** *Under the assumptions Eqs. (17)–(19), for all  $t \in \mathbb{R}$ ,*

$$\text{Im}[C(A, B, t)] = Q_{\rho,B}(e^{-iHt}U_{\text{Im}}). \quad (23)$$

*Moreover, if the initial state has definite parity, i.e.,  $P\rho = p\rho$  with  $p \in \{\pm 1\}$ , then*

$$\text{Re}[C(A, B, t)] = pQ_{\rho,B}(e^{-iHt}U_{\text{Re}}). \quad (24)$$

The full protocol is demonstrated in Algorithm 1 in the form of pseudocode.

Theorem 1 applies in particular when the initial state  $\rho$  is a non-degenerate eigenstate of  $H$ , in which case  $\rho$

---

**Algorithm 1** Tailored quench spectroscopy
 

---

**Input:** Initial state  $\rho$ , times  $t$ , Hamiltonian  $H$ , observables  $A, B$ , parity operator  $P$ , error bound  $\varepsilon$ .

**Output:** Estimate of  $C(A, B, t)$  with error bound  $\varepsilon$ .

- 1: Measure  $\rho$  in the eigenbasis of  $P$  to estimate its parity  $\hat{p}$ .
  - 2: **for**  $n = 1, 2, \dots, N = \mathcal{O}(\varepsilon^{-2})$  **do**
  - 3:   Prepare  $\rho$ ;
  - 4:   Apply quench operator  $U_{\text{Im}}$  on the state  $\rho$ ;
  - 5:   Let the state evolve under  $\exp(-iHt)$ ;
  - 6:   Measure the evolved state in the eigenbasis of  $B$  to obtain outcome  $c_n^{(i)}$ ;
  - 7: **end for**
  - 8: Compute  $\overline{c^{(i)}} = \sum_{n=1}^N c_n^{(i)}/N$ .
  - 9: **for**  $n = 1, 2, \dots, N = \mathcal{O}(\varepsilon^{-2})$  **do**
  - 10:   Prepare  $\rho$ ;
  - 11:   Apply quench operator  $U_{\text{Re}}$  on  $\rho$ ;
  - 12:   Let the state evolve under  $\exp(-iHt)$ ;
  - 13:   Measure the evolved state in the eigenbasis of  $B$  to obtain outcome  $c_n^{(r)}$ ;
  - 14: **end for**
  - 15: Compute  $\overline{c^{(r)}} = \sum_{n=1}^N c_n^{(r)}/N$ .
  - 16: Return  $\hat{p} \overline{c^{(r)}} + i \overline{c^{(i)}}$ .
- 

has a definite parity  $p \in \{\pm 1\}$ . In the degenerate case, since  $[H, P] = 0$ , one can choose an energy eigenbasis that simultaneously diagonalizes  $P$  within each degenerate eigenspace, and hence prepare a *pure* eigenstate with definite parity. In practice, parity can be assessed by estimating  $\langle P \rangle_\rho = \text{Tr}(\rho P)$  using standard end-of-circuit measurements. If parity leakage is observed (i.e.,  $|\langle P \rangle_\rho| < 1$ ), one may, for example, enforce a parity-preserving state-preparation circuit so that the prepared state remains within the desired parity sector. Since  $[H, P] = 0$ , parity is conserved under time evolution, so this calibration can be performed once and reused for subsequent quench spectroscopy runs.

Next, we show that an analogous strategy applies to thermal states. Consider a finite-temperature thermal (quantum Gibbs) state

$$\rho_\beta := \frac{e^{-\beta H}}{\mathcal{Z}}, \quad \mathcal{Z} := \text{Tr}(e^{-\beta H}), \quad (25)$$

at inverse temperature  $\beta$ . Since  $[H, P] = 0$ , it follows that  $[\rho_\beta, H] = [P, \rho_\beta] = 0$ . However,  $\rho_\beta$  generally does not have definite parity, i.e., it does not satisfy the stronger condition

$$P\rho_\beta = p\rho_\beta, \quad p \in \{\pm 1\}. \quad (26)$$

To recover a fixed-parity setting, we introduce the *symmetric and antisymmetric thermal states*, which correspond to the thermal state projected onto the even and

odd parity sectors:

$$\begin{aligned} \rho_S &= \frac{\Pi_S \rho_\beta \Pi_S}{\text{Tr}(\rho_\beta \Pi_S)} = \frac{\rho_\beta + \rho_\beta P}{1 + \text{Tr}(\rho_\beta P)} \\ \rho_A &= \frac{\Pi_A \rho_\beta \Pi_A}{\text{Tr}(\rho_\beta \Pi_A)} = \frac{\rho_\beta - \rho_\beta P}{1 - \text{Tr}(\rho_\beta P)}, \end{aligned} \quad (27)$$

where  $\Pi_S = (I + P)/2$  and  $\Pi_A = (I - P)/2$ .

These satisfy  $P\rho_S = \rho_S$  and  $P\rho_A = -\rho_A$ , and the original thermal state decomposes as

$$\rho_\beta = \frac{1 + \text{Tr}(\rho_\beta P)}{2} \rho_S + \frac{1 - \text{Tr}(\rho_\beta P)}{2} \rho_A. \quad (28)$$

With these definitions, TQS provides an efficient route to estimating the real component of  $C(A, B, t)$ , as summarized in the following theorem; see Appendix B3 for its proof.

**Theorem 2.** *Let  $\rho_\beta$ ,  $\rho_S$ , and  $\rho_A$  denote the thermal, symmetric, and antisymmetric thermal states of  $H$  at inverse temperature  $\beta$ . Under the assumptions Eqs. (17) and (18), for all  $t \in \mathbb{R}$ ,*

$$\begin{aligned} \text{Re}[C(A, B, t)] &= \frac{1 + \text{Tr}(\rho_\beta P)}{2} Q_{\rho_S, B}(e^{-iHt} U_{\text{Re}}) \\ &\quad - \frac{1 - \text{Tr}(\rho_\beta P)}{2} Q_{\rho_A, B}(e^{-iHt} U_{\text{Re}}), \end{aligned} \quad (29)$$

and the imaginary component can be estimated analogously to Theorem 1.

## B. Preparation of $\rho_S, \rho_A$

Since thermal-state preparation itself is a challenging task on near-term hardware, we treat the generation of parity-resolved Gibbs states as an input primitive: our TQS protocol applies to any procedure that can prepare  $\rho_S$  and  $\rho_A$  (exactly or approximately). Nevertheless, we outline two possible approaches. Measuring  $\rho_\beta$  with the two-outcome POVM  $\{\Pi_S, \Pi_A\}$  provides a conceptually simple way to obtain  $\rho_S$  and  $\rho_A$ . However, since  $P$  and  $B$  anticommute, a direct parity measurement is not compatible with the subsequent measurement in the eigenbasis of  $B$  within the same experimental run without additional overhead (e.g., ancilla-assisted parity checks with feed-forward and/or post-selection). Moreover, mid-circuit measurements are typically slow and noisy, making this approach less attractive.

Alternatively, we introduce a tailored *symmetric quantum Gibbs sampler* based on dissipative state preparation, which can directly prepare parity-resolved Gibbs states without requiring mid-circuit measurements. We first briefly review a Lindbladian framework for preparing Gibbs states via dissipative evolution that has seen renewed recent interest [34–36]. Let  $\mathcal{L}$  be a Lindbladian and consider the master equation

$$\frac{d}{dt} \rho(t) = \mathcal{L}[\rho(t)]. \quad (30)$$

Let  $\rho(t) = e^{\mathcal{L}t}[\rho(0)]$  denote the solution of the master equation. If the map  $e^{\mathcal{L}t}$  is *ergodic* [37], then there exists a unique steady state (in the context of quantum Gibbs sampler, the steady state is  $\rho_\beta$ ) such that  $\lim_{t \rightarrow \infty} \rho(t) = \rho_\beta$  for any initial state  $\rho(0)$ . In this way, Gibbs-state preparation is reduced to simulating dissipative dynamics.

A canonical construction is the *Davies generator*. Fix a system operator  $J$  and define its *Bohr-frequency components* (i.e., components labeled by energy gaps  $\nu = E_m - E_n$ ) by

$$J_\nu := \lim_{T \rightarrow \infty} \frac{1}{2T} \int_{-T}^T dt e^{iHt} J e^{-iHt} e^{-i\nu t}, \quad (31)$$

so that  $e^{iHt} J e^{-iHt} = \sum_\nu J_\nu e^{i\nu t}$ . Let  $\eta(\nu)$  be any function satisfying the relation  $\eta(\nu) = e^{\beta\nu} \eta(-\nu)$ . Then the Davies generator is defined as

$$\mathcal{L}_D[\cdot] = \sum_\nu \eta(\nu) \left[ J_\nu(\cdot) J_\nu^\dagger - \frac{1}{2} \{ J_\nu^\dagger J_\nu, \cdot \} \right]. \quad (32)$$

This Davies generator satisfies the Kubo-Martin-Schwinger (KMS) detailed balance condition [36] with respect to  $\rho_\beta$ :

$$\mathcal{L}_D[\cdot] = \rho_\beta^{1/2} \mathcal{L}_D^\dagger \left[ \rho_\beta^{-1/2} \cdot \rho_\beta^{-1/2} \right] \rho_\beta^{1/2}. \quad (33)$$

which implies  $\mathcal{L}_D[\rho_\beta] = 0$ . A self-consistent derivation is included in Appendix A 3.

To ensure that  $\rho_\beta$  is the *unique* steady state on the full Hilbert space, one imposes an irreducibility condition. One convenient formulation is via reducing projectors: a projector  $\Pi$  *reduces*  $\mathcal{L}_D$  if the corresponding subspace is invariant under the dynamics, namely

$$\mathcal{L}_D[\Pi\rho\Pi] = \Pi \mathcal{L}_D[\Pi\rho\Pi] \Pi, \quad \forall \rho. \quad (34)$$

If the only reducing projectors are  $\Pi = 0$  and  $\Pi = I$ , then  $\mathcal{L}_D$  is *irreducible* [38]; under additional mild assumptions (e.g., full rank of the stationary state), this implies a unique full-rank stationary state, which must be  $\rho_\beta$  by detailed balance.

In our application, however, we do not need global irreducibility. Instead, we want the dynamics to *preserve parity* so that it does not mix the even and odd sectors, and then be ergodic *within each sector*. This yields the parity-resolved Gibbs states  $\rho_S$  and  $\rho_A$  as the long-time limits.

Assuming  $[H, P] = 0$ , if we choose a jump operator that commutes with parity,  $[J, P] = 0$ , then the Davies dynamics is block-diagonal in the parity decomposition.

**Proposition 1.** *Suppose  $[H, P] = 0$  and  $[J, P] = 0$ . Then both  $\Pi_S$  and  $\Pi_A$  reduce the Davies generator  $\mathcal{L}_D$ .*

*Proof.* Since  $[H, P] = 0$ , we have  $e^{iHt} P e^{-iHt} = P$ . If  $[J, P] = 0$ , then  $[J(t), P] = 0$  for all  $t$ , where  $J(t) = e^{iHt} J e^{-iHt}$ . Taking Fourier components implies  $[J_\nu, P] = 0$  for all  $\nu$ , hence  $[J_\nu, \Pi_S] = [J_\nu, \Pi_A] = 0$ .

Let  $\sigma$  be supported in the even sector, i.e.,  $\sigma = \Pi_S \sigma \Pi_S$ . Then for each  $\nu$ ,

$$J_\nu \sigma J_\nu^\dagger = J_\nu (\Pi_S \sigma \Pi_S) J_\nu^\dagger = \Pi_S (J_\nu \sigma J_\nu^\dagger) \Pi_S, \quad (35)$$

$$J_\nu^\dagger J_\nu \sigma = J_\nu^\dagger J_\nu (\Pi_S \sigma \Pi_S) = \Pi_S (J_\nu^\dagger J_\nu \sigma) \Pi_S, \quad (36)$$

and similarly for  $\sigma J_\nu^\dagger J_\nu$ . Plugging these relations into Eq. (32) yields  $\mathcal{L}_D[\sigma] = \Pi_S \mathcal{L}_D[\sigma] \Pi_S$ , i.e.,  $\Pi_S$  reduces  $\mathcal{L}_D$ . The same argument applies to  $\Pi_A$ .  $\square$

The proposition implies that there is no transition between  $\mathcal{H}_{\text{even}}$  and  $\mathcal{H}_{\text{odd}}$  in the dissipative dynamics. Because the parity sectors are invariant, the long-time limit of the dynamics depends on the initial parity weights. In particular, if the restriction of  $\mathcal{L}_D$  to  $\mathcal{H}_{\text{even}}$  is ergodic, then the unique stationary state within that sector is the even-parity Gibbs state  $\rho_S$ ; likewise, ergodicity on  $\mathcal{H}_{\text{odd}}$  yields  $\rho_A$ . Thus, by preparing an initial state supported in the desired sector and evolving under a parity-preserving Davies generator that is ergodic within that sector, we obtain  $\rho_S$  or  $\rho_A$  without mid-circuit parity measurements.

In practice, Lindbladian evolution of this type can be implemented using dissipative dynamics and related simulation primitives [39, 40]. While some implementations introduce additional ancilla qubits, they avoid long-range controlled unitaries and deep interference structures, making them potentially suitable for near-term or early fault-tolerance quantum devices.

We now illustrate how to construct a parity-preserving Lindbladian whose unique steady state is the symmetric thermal state. As a concrete example, we consider the  $N = 4$  site XXZ model in Eq. (8) with parameters  $J_X = 2$ ,  $J_Z = 1$ , and  $h_Z = 10$ . To generate the full thermal state  $\rho_\beta$ , we choose a parity-breaking jump operator  $J = X_0$ . To generate the symmetric thermal state  $\rho_S$ , we instead choose the parity-preserving two-site operator  $J = Y_0 Y_1$ . We denote the corresponding Davies generators by  $\mathcal{L}_D$  (for  $J = X_0$ ) and  $\mathcal{L}_{D,S}$  (for  $J = Y_0 Y_1$ ).

To simulate the Lindbladian dynamics, we vectorize the density matrix using the Pauli basis. Let  $\mathcal{P}_n = \{P_i\}_{i=0}^{d^2-1}$  be the set of  $n$ -qubit Pauli operators (including the identity), where  $d = 2^n$ . We define the vectorization of  $\rho$  as

$$|\rho\rangle\rangle = \frac{1}{d} \sum_{i=0}^{d^2-1} \text{Tr}(\rho P_i) e_i, \quad (37)$$

with  $\{e_i\}_{i=0}^{d^2-1}$  the standard basis of  $\mathbb{R}^{d^2}$ . Under this mapping, the action of a Lindbladian  $\mathcal{L}$  becomes a matrix  $\hat{\mathcal{L}}$  acting linearly on  $|\rho\rangle\rangle$ , i.e.,

$$\begin{aligned} |\mathcal{L}(\rho)\rangle\rangle &= \frac{1}{d} \sum_{i=0}^{d^2-1} \text{Tr}(\mathcal{L}(\rho) P_i) e_i = \frac{1}{d} \sum_{i=0}^{d^2-1} \text{Tr}(\rho \mathcal{L}^\dagger(P_i)) e_i \\ &= \hat{\mathcal{L}} |\rho\rangle\rangle, \end{aligned} \quad (38)$$

where

$$\begin{aligned}\hat{L} &= \frac{1}{d} \sum_{i,j=0}^{d^2-1} \text{Tr}(\mathcal{L}^\dagger(P_i)P_j) e_i e_j^\top \\ &= \frac{1}{d} \sum_{i,j=0}^{d^2-1} \text{Tr}(P_i \mathcal{L}(P_j)) e_i e_j^\top.\end{aligned}\quad (39)$$

The Lindbladian equation thus becomes the linear ODE

$$\frac{d}{dt} |\rho(t)\rangle\rangle = \hat{L} |\rho(t)\rangle\rangle. \quad (40)$$

We initialize  $\rho(0)$  as a random state supported in the even-parity subspace and evolve under both generators. As shown in Fig. 2, the distance to the corresponding steady state decays at comparable rates for  $e^{\mathcal{L}_D t}$  and  $e^{\mathcal{L}_{D,S} t}$ , indicating similar mixing times in this example.

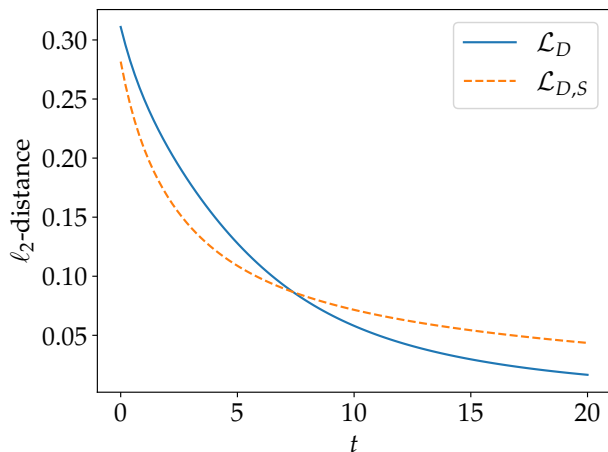


FIG. 2. Preparation of thermal states via Davies generators. The horizontal axis is the Lindbladian evolution time  $t$ , and the vertical axis is the  $\ell_2$ -distance between the vectorized evolved state and the corresponding steady state. The blue solid curve ( $\mathcal{L}_D$ ) shows convergence to a *regular thermal state*, while the orange dashed curve ( $\mathcal{L}_{D,S}$ ) shows convergence to a *symmetric thermal state*.

### C. Generalization to OTOC

Our approach can be partially extended to a class of  $n$ -point correlators [26, 41, 42]. Let  $O_0, O_1, \dots, O_L$  be  $L+1$  observables and consider the correlator

$$\text{Tr}(\rho O_0 O_1 \cdots O_L). \quad (41)$$

Assume the initial state is parity-symmetric,  $[\rho, P] = 0$ , and that  $O_0$  is parity-odd,  $\{O_0, P\} = 0$ . As in the two-point setting, we introduce the tailored quench operators

$$U_{\text{Im}} = \frac{I + iO_0}{\sqrt{2}}, \quad U_{\text{Re}} = \frac{P + O_0}{\sqrt{2}}. \quad (42)$$

We focus on the case where the remaining operators  $O_1, \dots, O_L$  are Heisenberg-evolved Pauli operators, i.e.,  $O_\ell = O_\ell(t_\ell) = e^{iHt_\ell} O_\ell e^{-iHt_\ell}$ , and the ordered product is invariant under reversal,

$$O_1 O_2 \cdots O_L = O_L \cdots O_2 O_1, \quad (43)$$

which holds, for example, for certain palindromic strings arising in out-of-time-order correlators. Under these conditions, the same TQS measurement primitives can be used to access the desired correlator.

A particularly important example is the out-of-time-order correlator (OTOC), widely used to diagnose quantum chaos and information scrambling [43, 44]. For a thermal state  $\rho_\beta$  and Pauli operators  $A, B$ , we define

$$\text{OTOC}(A, B, t) = \text{Tr}[\rho_\beta A B(t) A B(t)], \quad (44)$$

where  $B(t) = e^{iHt} B e^{-iHt}$ . Introduce the operator  $\tilde{A} := B e^{-iHt} A e^{iHt} B$ . Then its Heisenberg evolution satisfies

$$\tilde{A}(t) = e^{iHt} \tilde{A} e^{-iHt} = B(t) A B(t), \quad (45)$$

and therefore

$$\text{OTOC}(A, B, t) = \text{Tr}[\rho_\beta A \tilde{A}(t)] \equiv C(A, \tilde{A}, t), \quad (46)$$

where we use the convention  $C(X, Y, t) = \text{Tr}(\rho_\beta X Y(t))$ . Experimentally, this reduces to estimating the modified quench functions

$$Q_{\rho_\beta, A}(e^{iHt} B e^{-iHt} U_{\text{Im/Re}}). \quad (47)$$

The full quantum circuit is shown in Fig. 3.

## IV. COMPLEXITY AND ERROR ANALYSIS

### A. Complexity analysis

For a fixed time  $t$ , estimating  $C(A, B, t)$  (or its real/imaginary parts) reduces to estimating a constant number of quench functions. Therefore, to achieve additive error  $\varepsilon$  with constant success probability, the number of shots per time point scales as  $\mathcal{O}(\varepsilon^{-2})$  by standard concentration bounds.

To reconstruct the Green's function  $G(z)$ , one must resolve the frequency content of the measured time-domain correlator. For sparse line spectra, classical signal processing methods such as MULTIPLE SIGNAL CLASSIFICATION (MUSIC) [45] can estimate frequencies from samples  $C(A, B, t_m)$  taken over a time window of length  $T_{\text{max}}$ . Resolving spectral components separated by a minimum gap  $\Delta f$  generally requires an observation time  $T_{\text{max}} = \mathcal{O}(\Delta f^{-1})$ . Using  $M$  time samples with step size  $\delta t$ , we have  $M \approx T_{\text{max}}/\delta t$ , so  $M = \mathcal{O}(\Delta f^{-1} \delta t^{-1})$ . Since each time point requires  $\mathcal{O}(\varepsilon^{-2})$  shots to estimate the relevant quench expectation values to additive error  $\varepsilon$ , the total number of circuit executions scales as

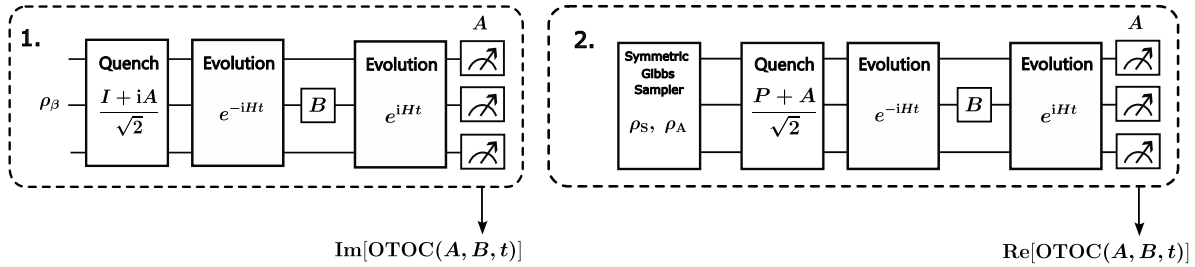


FIG. 3. Quantum circuits for estimating  $\text{OTOC}(A, B, t)$  using tailored quench spectroscopy.

$\mathcal{O}(M\varepsilon^{-2}) = \mathcal{O}(\Delta f^{-1}\delta t^{-1}\varepsilon^{-2})$ , up to logarithmic factors and constants depending on the noise level.

For thermal Green's functions, a natural lower bound on the smallest frequency scale is set by energy differences  $|E_m - E_n|$ , so the relevant gap is controlled by  $\min_{m \neq n} |E_m - E_n|$  (or by the subset of transitions with non-negligible spectral weight).

### B. Error analysis

In the nonequilibrium setting, an error in the prepared initial state translates directly into an error in the correlator: since  $C(A, B, t)$  is linear in  $\rho$ , the deviation is bounded by the trace distance  $\|\rho - \rho_{\text{ideal}}\|_1$  (up to an operator-norm factor). In the equilibrium setting, we can further suppress symmetry-breaking preparation errors by applying a *symmetrization channel*

$$\mathcal{S}(\rho) = \frac{\rho + P\rho P}{2}, \quad (48)$$

which removes coherences between opposite parity sectors.

To illustrate the effect, suppose the ideal initial state is the ground state  $|0\rangle$  and the actual prepared state is

$$|\psi\rangle = \alpha|0\rangle + \mu|1\rangle, \quad |\mu| \ll 1, \quad (49)$$

where  $|1\rangle$  has opposite parity to  $|0\rangle$ . The corresponding error contribution to the estimator can be written as

$$\begin{aligned} & \frac{1}{2}\langle\psi|B(t)|\psi\rangle + \frac{1}{2}\langle\psi|AB(t)A|\psi\rangle \\ & + \frac{1}{2}\langle\psi|i[A, B(t)]|\psi\rangle - \frac{1}{2}\langle 0|i[A, B(t)]|0\rangle. \end{aligned} \quad (50)$$

Here  $i[A, B(t)]$  is parity-even (symmetry-preserving), whereas  $B(t)$  and  $AB(t)A$  are parity-odd (symmetry-breaking) under the assumptions  $\{A, P\} = \{B, P\} = 0$ . Expanding in  $\mu$ , the error becomes

$$\begin{aligned} & \text{Re}[\alpha\mu^*\langle 1|B(t)|0\rangle] + \text{Re}[\alpha\mu^*\langle 1|AB(t)A|0\rangle] \\ & + \frac{|\mu|^2}{2}\langle 1|i[A, B(t)]|1\rangle - \frac{|\mu|^2}{2}\langle 0|i[A, B(t)]|0\rangle. \end{aligned} \quad (51)$$

The leading contribution is  $\mathcal{O}(|\mu|)$ .

After applying symmetrization, the effective state becomes the incoherent mixture

$$\mathcal{S}(|\psi\rangle\langle\psi|) = |\alpha|^2|0\rangle\langle 0| + |\mu|^2|1\rangle\langle 1|, \quad (52)$$

which removes the off-diagonal coherence terms responsible for the  $\mathcal{O}(|\mu|)$  contribution. As a result, the leading error is reduced to  $\mathcal{O}(|\mu|^2)$ .

### V. NUMERICAL SIMULATION

In this section, we present numerical experiments validating the TQS protocol and its robustness to state-preparation errors. To simulate real-time dynamics without ancillas, we use a first-order Trotter–Suzuki (TS) product formula [46, 47]. For a time-independent Hamiltonian  $H = \sum_{\gamma=1}^{\Gamma} H_{\gamma}$ , where each  $H_{\gamma}$  is a sum of mutually commuting Pauli terms, we approximate the time-evolution operator by

$$U_{\text{TS}}(t) := \left[ \prod_{\gamma=1}^{\Gamma} \exp(-iH_{\gamma} t/N_T) \right]^{N_T}, \quad (53)$$

where  $N_T$  is the number of Trotter steps (circuit layers) and directly controls circuit depth. For fixed  $t$ , the first-order TS error typically decreases as  $\mathcal{O}(\|H\|t^2/N_T)$ . Higher-order product formulas can further improve the asymptotic scaling in  $t$  and  $N_T$  [46, 47]. In our setting, if each term  $H_{\gamma}$  respects parity, i.e.,  $[H_{\gamma}, P] = 0$ , then  $U_{\text{TS}}(t)$  also commutes with  $P$ ; consequently, the simulated dynamics preserves parity and the symmetry-based conclusions of the previous sections continue to apply.

To model imperfect initial-state preparation, we generate a random mixed-state perturbation as follows. We first draw a random traceless Hermitian matrix  $E$  by sampling independent Gaussian entries (and enforcing Hermiticity), and normalize it to  $\tilde{E}$  such that  $\|\tilde{E}\|_1 = 1$ . We then define a full-rank state

$$\varrho := \frac{e^{\tilde{E}}}{\text{Tr}(e^{\tilde{E}})}. \quad (54)$$

Given a noise strength  $\varepsilon \in [0, 1]$ , we perturb the target initial state  $\rho$  by forming  $\rho + \varepsilon \tilde{\rho}$  and renormalizing to trace one, yielding  $\tilde{\rho}$ . This construction produces a controlled trace-distance deviation, with  $\|\rho - \tilde{\rho}\|_1$  typically of order  $\varepsilon$ .

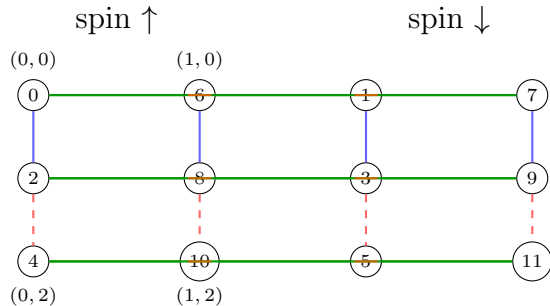
For our Green's function demonstrations, we consider a rescaled Fermi–Hubbard model (FHM) on a  $2 \times 3$  lattice with open boundary conditions, as shown in Fig. 4. The system contains 12 spin-orbitals, indexed by

$$(x, y, \uparrow) \mapsto 6x + 2y, \quad (x, y, \downarrow) \mapsto 6x + 2y + 1, \quad (55)$$

where  $x \in \{0, 1\}$  and  $y \in \{0, 1, 2\}$  label lattice sites. We rescale the Hamiltonian so that its spectral norm equals  $\pi$ , and decompose it into four commuting layers for TS simulation:

$$\begin{aligned} T_1 &= -\gamma \sum_{j \in \{0, 1, 6, 7\}} \left( c_j^\dagger c_{j+2} + c_{j+2}^\dagger c_j \right), \\ T_2 &= -\gamma \sum_{j \in \{2, 3, 8, 9\}} \left( c_j^\dagger c_{j+2} + c_{j+2}^\dagger c_j \right), \\ T_3 &= -\gamma \sum_{j=0}^5 \left( c_j^\dagger c_{j+6} + c_{j+6}^\dagger c_j \right), \\ T_4 &= \gamma h_U \sum_{j=0}^5 n_{2j} n_{2j+1}, \end{aligned} \quad (56)$$

with  $\gamma := \pi / \|H_{\text{FH}}\|$ .



$T_1$ : solid blue vertical bonds;  $T_2$ : dashed red vertical bonds;  $T_3$ : solid green intra- and inter-layer hoppings;  $T_4$ : orange bars on-site  $n_\uparrow n_\downarrow$ .

FIG. 4. Fermi–Hubbard model on a  $2 \times 3$  lattice. Each site  $(x, y)$  has spin- $\uparrow$  and spin- $\downarrow$  orbitals, mapped to indices  $j$  as  $(x, y, \uparrow) \mapsto 6x + 2y$  and  $(x, y, \downarrow) \mapsto 6x + 2y + 1$ .

After estimating the time-domain correlator  $C(A, B, t)$  on a discrete time grid, we reconstruct its frequency content using MUSIC, which builds a Hankel matrix from the sampled signal and decomposes it into a signal subspace and an orthogonal noise subspace. From the noise subspace one forms the MUSIC noise-subspace correlation function:

$$R(\omega) := \|U_{\text{noise}}^\dagger a(\omega)\|_2, \quad (57)$$

where  $a(\omega) = [e^{-i\omega n}]_{n=1}^N$  and  $U_{\text{noise}}$  spans the noise subspace; see Appendix C for more details. In the ideal noiseless case and with sufficient sampling,  $U_{\text{noise}}^\dagger a(\omega) = 0$  at the true frequencies. As plotted in our numerical results,  $R(\omega)$  therefore provides a direct and visually stable diagnostic of the recovered spectral support and its robustness under imperfections. Compared with directly Fourier transforming finite-time data, the MUSIC noise-subspace correlation function can resolve closely spaced frequencies beyond the naive Fourier limit when the signal is well-approximated by a sparse sum of exponentials.

Once the dominant frequencies  $\{\hat{f}_k\}$  are identified from the local minima of  $R(\omega)$ , one can estimate the corresponding amplitudes  $\{\hat{c}_k\}$  by a linear least-squares fit of the model  $s_n \approx \sum_{k=1}^K c_k e^{-if_k n}$  to the measured time samples. Finally, the many-body Green's function can be reconstructed by substituting the recovered frequencies and weights into the Lehmann form, i.e., as a sum of simple poles at the transition frequencies with residues determined by the fitted amplitudes.

## A. Ground states

In Fig. 5 and Fig. 6 we evaluate the ground-state time correlator  $C(A, B, t)$  that underlies the corresponding Green's function and benchmark against both exact evolution and first-order TS simulation. We consider two interaction regimes: a strongly correlated case ( $h_U = 6$ ) and a weakly interacting case ( $h_U = 0.1$ ), with  $A = B = (c_0 + c_0^\dagger)/2$ . Across both regimes, the reconstructed real and imaginary parts of the correlator remain stable under moderate initial-state preparation error and under Trotterization at the chosen step size. Moreover, the noise-subspace correlation function  $R(\omega)$  computed from the noisy data closely matches its exact counterpart, indicating that the signal-processing stage is robust to the state-preparation perturbations and Trotter errors considered here.

## B. Finite-temperature thermal states

Figures 7 and 8 extend the same analysis to finite temperature with  $\beta = 1$ . In contrast to the ground-state setting, the correlator receives contributions from multiple energy differences weighted by thermal populations, which generally increases spectral congestion. Nevertheless, the TQS estimator continues to yield accurate real and imaginary components of  $C(A, A, t)$  in both interaction regimes. These results support the practicality of the symmetry-enabled protocol for probing equilibrium dynamics beyond zero temperature, provided that the parity symmetry condition is satisfied and the thermal-state preparation error remains controlled.

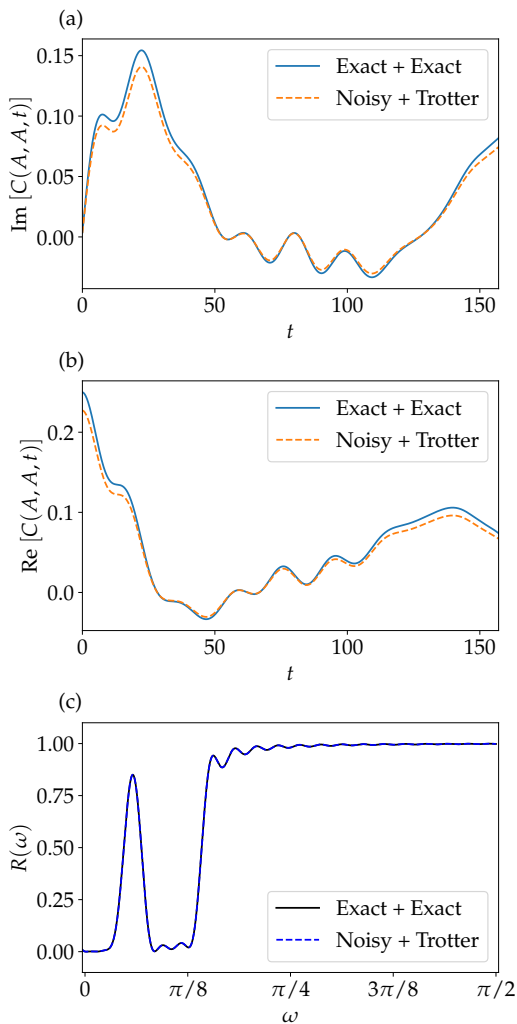


FIG. 5. Ground-state numerical simulations for the 2D Fermi-Hubbard model on a  $2 \times 3$  lattice with open boundary conditions. The interaction strength is  $h_U = 6$ . The observable is  $A = B = (c_0 + c_0^\dagger)/2$ . The system is evolved up to time  $200\pi$  with a Trotter step of  $\pi/20$  (only the region  $t \in [0, 50\pi]$  is shown). Initial-state preparation error is modeled by perturbing the initial state once as  $\tilde{\rho} = (\rho + \varepsilon\varrho)/\text{Tr}(\rho + \varepsilon\varrho)$  with  $\varepsilon = 0.1$  and a fixed random state  $\varrho$ . In the legend, the first “Exact” denotes an exact initial state, the second “Exact” denotes exact time evolution; “Noisy” corresponds to using the perturbed initial state  $\tilde{\rho}$ ; and “Trotter” refers to simulation via the TS decomposition. (a) Imaginary part of  $C(A, B, t)$  as a function of time. (b) Real part of  $C(A, B, t)$ . (c) Noise-subspace correlation function  $R(\omega)$  for  $\omega \in [0, \pi/2]$ , constructed from the sampled time signal.

### C. Finite-temperature OTOCs

Figure 9 demonstrates the generalization of TQS to out-of-time-ordered correlators (OTOCs) using the 1D XXZ chain in Eq. (8). We choose  $J_X = 1$ ,  $J_Z = 2$ , and  $h = 1$ , corresponding to an anisotropy  $\Delta = J_Z/J_X = 2 > 1$  with a longitudinal field that breaks integrabil-

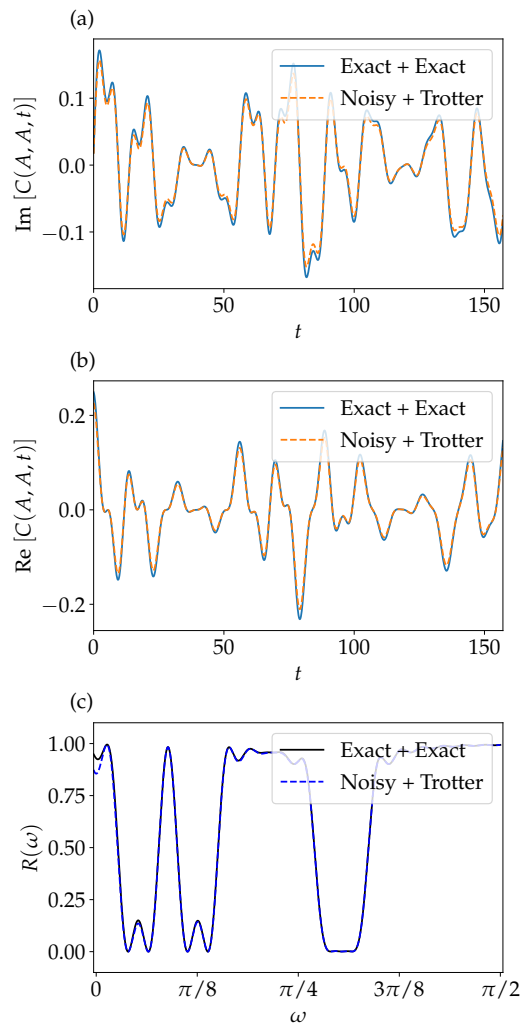


FIG. 6. Ground-state numerical simulations for the 2D Fermi-Hubbard model on a  $2 \times 3$  lattice with open boundary conditions. The setup and the meaning of the subplots are the same as Fig. 5, except the interaction strength is  $h_U = 0.1$ .

ity. This regime exhibits interacting, nontrivial dynamics and provides a representative setting to test the stability of OTOC estimation under Trotterization and state-preparation imperfections.

## VI. CONCLUSION AND OUTLOOK

We introduced a symmetry-enabled direct quantum protocol, tailored quench spectroscopy (TQS), for computing both the real and imaginary parts of two-point time correlators without controlled unitaries or ancilla qubits in the correlator-estimation circuit. The central observation is that when a parity operator  $P$  commutes with the Hamiltonian and the observables of interest are parity-odd, symmetry enforces selection rules that simplify quench spectroscopy readout. For fixed-parity initial states (including energy eigenstates) the correlator

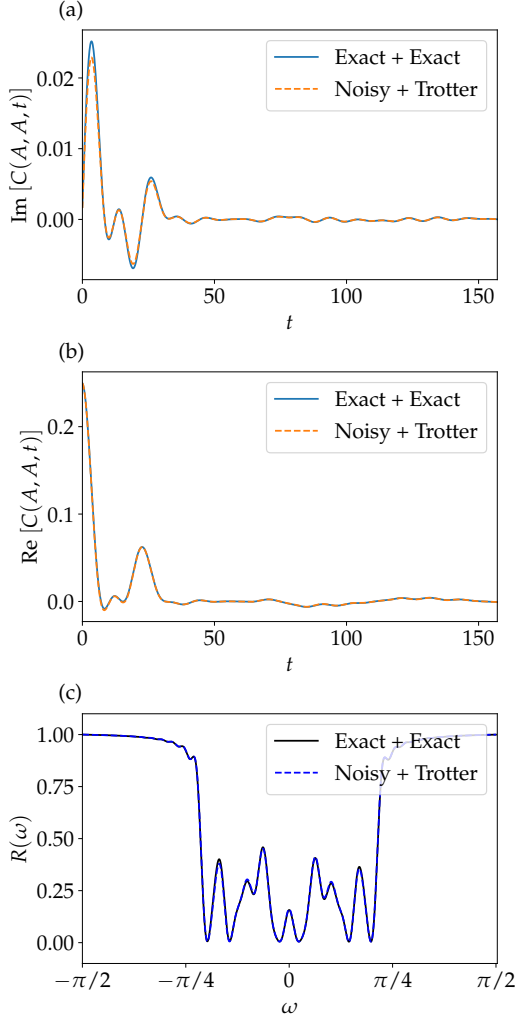


FIG. 7. Finite-temperature numerical simulations for the 2D Fermi-Hubbard model on a  $2 \times 3$  lattice with open boundary conditions. The setup and the meaning of the subplots are the same as Fig. 5, except the initial state is the thermal state  $\rho_\beta$  with  $\beta = 1$  and the interaction strength is  $h_U = 6$ .

can be obtained from only two quench functions, and for thermal states we showed how to combine parity-resolved correlators obtained from symmetric and antisymmetric Gibbs states. Together with classical signal processing (e.g., MUSIC), these correlators yield the Lehmann representation of the Green’s function. Our error analysis highlights that symmetry-based symmetrization can quadratically suppress parity-breaking state-preparation errors. Numerical simulations on Fermi-Hubbard and XXZ instances support the robustness of the approach under Trotterization and imperfect state preparation. Finally, we demonstrated that the same symmetry-based measurement primitive extends to a class of multi-point correlators, including OTOCs.

This work opens several new exciting directions. First, it is natural to ask how far symmetry-enabled direct protocols can be extended beyond linear two-point re-

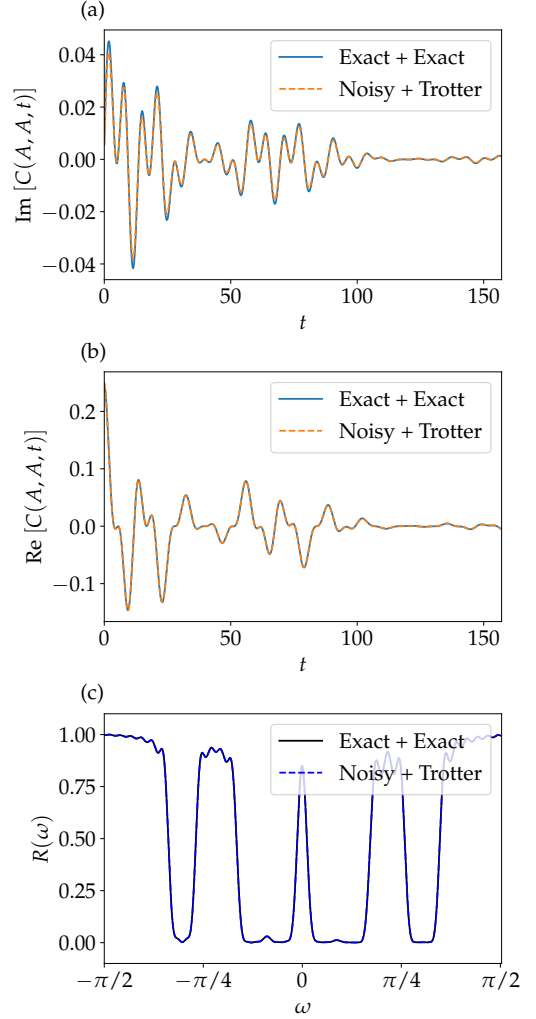


FIG. 8. Finite-temperature numerical simulations for the 2D Fermi-Hubbard model on a  $2 \times 3$  lattice with open boundary conditions. The setup and the meaning of the subplots are the same as Fig. 5, except the interaction strength is  $h_U = 0.1$ .

sponse. One avenue is the measurement of higher-order and nonlinear response functions [48], where parity constraints might reduce the overhead of accessing specific operator orderings or nested commutators. A related question is whether analogous ideas can be adapted to non-Hermitian [49, 50] or effective open-system settings, e.g., when the dynamics is generated by a non-Hermitian Hamiltonian or by a Lindbladian, where Green’s functions and response theory take modified forms and symmetry constraints may still yield simplifications.

Second, a near-term priority is experimental demonstration. Because TQS requires only native time evolution under a time-independent Hamiltonian and end-of-circuit measurements, it is compatible with both digital platforms and analog simulators, where quench-style protocols are natural. A promising first milestone is a hardware demonstration of parity-assisted recovery of  $\text{Re}[C(A, B, t)]$  and  $\text{Im}[C(A, B, t)]$  in small Hubbard

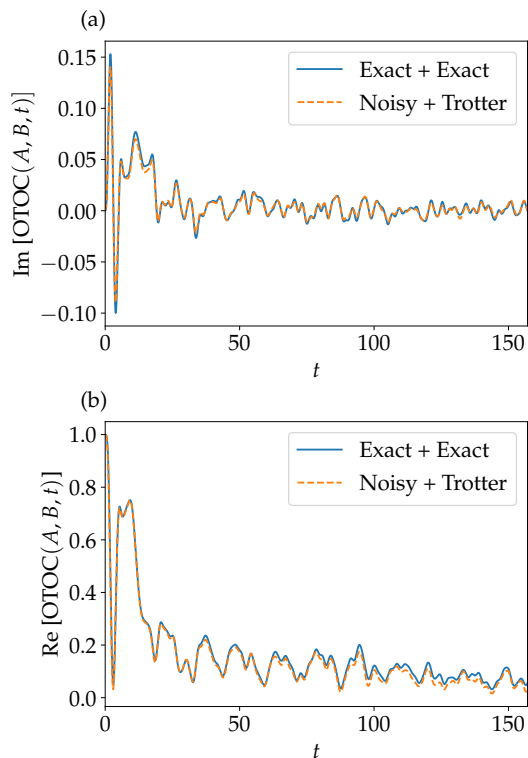


FIG. 9. Real and imaginary components of the OTOC for the 1D XXZ model [see Eq. (8)] on  $N = 8$  sites with open boundary conditions. The parameters are  $J_X = 1$ ,  $J_Z = 2$ , and  $h = 1$ . The local observables are  $A = X_0$  and  $B = Z_2$ . The initial state is the thermal state  $\rho_\beta$  with  $\beta = 1$ . The remaining setup and the meaning of the subplots are similar to those in Fig. 5.

or spin-chain instances, followed by reconstruction of low-lying spectral features via classical signal analysis. Benchmarking the protocol under realistic noise and comparing against other available approaches would clarify the practical advantage of symmetry-enabled direct mea-

surement.

Finally, several technical questions remain open. On the theory side, sharper sample-complexity guarantees for signal reconstruction under realistic noise (including state-preparation and measurement noise) would strengthen the end-to-end performance picture. On the implementation side, developing more efficient and hardware-tailored preparation methods for parity-resolved thermal states, possibly avoiding dissipative overhead in some settings, would broaden the applicability of finite-temperature TQS. We expect that exploring these directions will further establish symmetry-enabled direct protocols as practical tools for probing finite-temperature dynamics of strongly correlated quantum matter.

#### ACKNOWLEDGEMENT

C.Y. acknowledges support from the National Key Research and Development Program of China (Grant No. 2022YFA1404204), Shanghai Municipal Science and Technology Major Project (Grant No. 2019SHZDZX01), National Natural Science Foundation of China (Grant No. 92165109), and Shanghai Municipal Science and Technology Major Project (Grant No. 2019SHZDZX01-ZX04). C.Z. acknowledges support from the Faculté des sciences and Institut quantique at Université de Sherbrooke, as well as from the Institut transdisciplinaire d'information quantique (INTRIQ), a strategic cluster funded by the Fonds de recherche du Québec – Nature et technologies. We sincerely thank Dr. Mario Motta and Dr. Alexandre Foley for their careful reading of our draft and for the numerous insightful comments they provided.

#### DATA AVAILABILITY

The data and code supporting the findings of this work are available at [51].

- 
- [1] A. Altland and B. D. Simons, *Condensed matter field theory* (Cambridge University Press, Cambridge, UK, 2010).
  - [2] H. Zhang, T. Pincelli, C. Jozwiak, T. Kondo, R. Ernstorfer, T. Sato, and S. Zhou, Angle-resolved photoemission spectroscopy, *Nat. Rev. Methods Primers* **2**, 54 (2022).
  - [3] L. J. P. Ament, M. van Veenendaal, T. P. Devereaux, J. P. Hill, and J. van den Brink, Resonant inelastic X-ray scattering studies of elementary excitations, *Rev. Mod. Phys.* **83**, 705 (2011).
  - [4] V. Viswanath and G. Müller, *The recursion method: application to many body dynamics*, Vol. 23 (Springer Science & Business Media, Berlin, Germany, 1994).
  - [5] W. M. Foulkes, L. Mitas, R. Needs, and G. Rajagopal, Quantum Monte Carlo simulations of solids, *Rev. Mod. Phys.* **73**, 33 (2001).
  - [6] G. Vidal, Efficient simulation of one-dimensional quantum many-body systems, *Phys. Rev. Lett.* **93**, 040502 (2004).
  - [7] B. Bauer, D. Wecker, A. J. Millis, M. B. Hastings, and M. Troyer, Hybrid quantum-classical approach to correlated materials, *Phys. Rev. X* **6**, 031045 (2016).
  - [8] I. Loaiza, D. Motlagh, K. Hejazi, M. S. Zini, A. Delgado, and J. M. Arrazola, Nonlinear spectroscopy via generalized quantum phase estimation, *Quantum* **9**, 1822 (2025).
  - [9] J. Sun, L. Vilchez-Estevéz, V. Vedral, A. T. Boothroyd, and M. Kim, Probing spectral features of quantum many-body systems with quantum simulators, *Nat. Commun.* **16**, 1 (2025).
  - [10] E. Cruz, D. S. Wild, M. C. Bañuls, and J. I. Cirac, Quantum simulation of dynamical response functions of equilibrium states, *Phys. Rev. A* **112**, 032610 (2025).
  - [11] M. L. Baez, M. Goihl, J. Haferkamp, J. Bermejo-Vega, M. Gluza, and J. Eisert, Dynamical structure factors of dynamical quantum simulators, *Proc. Natl. Acad. Sci. U.*

- S. A. **117**, 26123 (2020).
- [12] D. Cruz and D. Magano, Superresolution of Green's functions on noisy quantum computers, *Phys. Rev. A* **108**, 012618 (2023).
- [13] H. Chen, M. Nusspickel, J. Tilly, and G. H. Booth, Variational quantum eigensolver for dynamic correlation functions, *Phys. Rev. A* **104**, 032405 (2021).
- [14] K. Huang, X. Cai, H. Li, Z.-Y. Ge, R. Hou, H. Li, T. Liu, Y. Shi, C. Chen, D. Zheng, *et al.*, Variational quantum computation of molecular linear response properties on a superconducting quantum processor, *J. Phys. Chem. Lett.* **13**, 9114 (2022).
- [15] D. Dhawan, D. Zgid, and M. Motta, Quantum algorithm for imaginary-time Green's functions, *J. Chem. Theory Comput.* **20**, 4629 (2024).
- [16] J. Preskill, Quantum computing in the NISQ era and beyond, *Quantum* **2**, 79 (2018).
- [17] A. Katabarwa, K. Gratsea, A. Caesura, and P. D. Johnson, Early fault-tolerant quantum computing, *PRX Quantum* **5**, 020101 (2024).
- [18] M. Knap, A. Kantian, T. Giamarchi, I. Bloch, M. D. Lukin, and E. Demler, Probing real-space and time-resolved correlation functions with many-body Ramsey interferometry, *Phys. Rev. Lett.* **111**, 147205 (2013).
- [19] Y. Yang, Y. Li, X. Xu, and X. Yuan, Resource-efficient quantum-classical hybrid algorithm for energy gap evaluation, *Phys. Rev. A* **109**, 052416 (2024).
- [20] L. Villa, J. Despres, and L. Sanchez-Palencia, Unraveling the excitation spectrum of many-body systems from quantum quenches, *Phys. Rev. A* **100**, 063632 (2019).
- [21] E. Kökcü, H. A. Labib, J. Freericks, and A. F. Kemper, A linear response framework for quantum simulation of bosonic and fermionic correlation functions, *Nat. Commun.* **15**, 3881 (2024).
- [22] S. Piccinelli, F. Tacchino, I. Tavernelli, and G. Carleo, Efficient calculation of Green's functions on quantum computers via simultaneous circuit perturbation (2025), arXiv:2505.05563 [quant-ph].
- [23] G. Bishop, D. Bagrets, and F. K. Wilhelm, Quantum algorithm for Green's-function measurements in the Fermi-Hubbard model, *Phys. Rev. A* **111**, 062610 (2025).
- [24] M. Motta, C. Sun, A. T. Tan, M. J. O'Rourke, E. Ye, A. J. Minnich, F. G. Brandao, and G. K.-L. Chan, Determining eigenstates and thermal states on a quantum computer using quantum imaginary time evolution, *Nat. Phys.* **16**, 205 (2020).
- [25] Y. Yang, A. Christianen, M. C. Bañuls, D. S. Wild, and J. I. Cirac, Phase-sensitive quantum measurement without controlled operations, *Phys. Rev. Lett.* **132**, 220601 (2024).
- [26] X. Wang, L. Xiong, X. Cai, and X. Yuan, Computing  $n$ -time correlation functions without ancilla qubits, *Phys. Rev. Lett.* **135**, 230602 (2025).
- [27] G. Greene-Diniz, D. Z. Manrique, K. Yamamoto, E. Plekhanov, N. Fitzpatrick, M. Krompiec, R. Sakuma, and D. M. Ramo, Quantum computed Green's functions using a cumulant expansion of the Lanczos method, *Quantum* **8**, 1383 (2024).
- [28] R. Irmejs and R. A. Santos, Approximating dynamical correlation functions with constant depth quantum circuits, *Quantum* **9**, 1639 (2025).
- [29] E. N. Epperly, L. Lin, and Y. Nakatsukasa, A theory of quantum subspace diagonalization, *SIAM Journal on Matrix Analysis and Applications* **43**, 1263–1290 (2022).
- [30] K. Mitarai and K. Fujii, Methodology for replacing indirect measurements with direct measurements, *Phys. Rev. Res.* **1**, 013006 (2019).
- [31] M. M. Odashima, B. G. Prado, and E. Vernek, Pedagogical introduction to equilibrium Green's functions: condensed-matter examples with numerical implementations, *Revista Brasileira de Ensino de Física* **39**, 10.1590/1806-9126-RBEF-2016-0087 (2016).
- [32] L. Villa, *Out-of-equilibrium dynamics and quench spectroscopy of ultracold many-body quantum systems*, Ph.D. thesis, Institut Polytechnique de Paris (2021).
- [33] J. Haah, Y. Liu, and X. Tan, Efficient approximate unitary designs from random Pauli rotations, *Communications in Mathematical Physics* **406**, 1 (2025).
- [34] C.-F. Chen, M. J. Kastoryano, F. G. S. L. Brandão, and A. Gilyéns, Efficient quantum thermal simulation, *Nature* **646**, 561 (2025).
- [35] Y. Tong and Y. Zhan, Fast mixing of weakly interacting fermionic systems at any temperature, *PRX Quantum* **6**, 030301 (2025).
- [36] Z. Ding, B. Li, and L. Lin, Efficient quantum Gibbs samplers with Kubo–Martin–Schwinger detailed balance condition, *Commun. Math. Phys.* **406**, 67 (2025).
- [37] H.-P. Breuer and F. Petruccione, *The theory of open quantum systems* (OUP Oxford, 2002).
- [38] Y. Zhang and T. Barthel, Criteria for Davies irreducibility of Markovian quantum dynamics, *J. Phys. A: Math. Theor.* **57**, 115301 (2024).
- [39] Z. Ding, C.-F. Chen, and L. Lin, Single-ancilla ground state preparation via Lindbladians, *Phys. Rev. Res.* **6**, 033147 (2024).
- [40] W. Yu, X. Li, Q. Zhao, and X. Yuan, Lindbladian simulation with logarithmic precision scaling via two ancillas, *Phys. Rev. Lett.* **135**, 160602 (2025).
- [41] J. S. Pedernales, R. Di Candia, I. L. Egusquiza, J. Casanova, and E. Solano, Efficient quantum algorithm for computing  $n$ -time correlation functions, *Phys. Rev. Lett.* **113**, 020505 (2014).
- [42] L. Del Re, B. Rost, M. Foss-Feig, A. Kemper, and J. Freericks, Robust measurements of  $n$ -point correlation functions of driven-dissipative quantum systems on a digital quantum computer, *Phys. Rev. Lett.* **132**, 100601 (2024).
- [43] K. Hashimoto, K. Murata, and R. Yoshii, Out-of-time-order correlators in quantum mechanics, *J. High Energy Phys.* **2017** (10), 1.
- [44] I. García-Mata, R. Jalabert, and D. Wisniacki, Out-of-time-order correlations and quantum chaos, *Scholarpedia* **18**, 55237 (2023).
- [45] W. Liao and A. Fannjiang, MUSIC for single-snapshot spectral estimation: Stability and super-resolution, *Appl. Comput. Harmon. Anal.* **40**, 33 (2016).
- [46] A. M. Childs and Y. Su, Nearly optimal lattice simulation by product formulas, *Phys. Rev. Lett.* **123**, 050503 (2019).
- [47] A. M. Childs, Y. Su, M. C. Tran, N. Wiebe, and S. Zhu, Theory of Trotter error with commutator scaling, *Phys. Rev. X* **11**, 011020 (2021).
- [48] A. Ono, Extracting nonlinear dynamical response functions from time evolution, *Phys. Rev. Lett.* **135**, 026401 (2025).
- [49] L. Pan, X. Chen, Y. Chen, and H. Zhai, Non-Hermitian linear response theory, *Nat. Phys.* **16**, 767 (2020).

[50] K. T. Geier and P. Hauke, From non-Hermitian linear response to dynamical correlations and fluctuation-dissipation relations in quantum many-body systems,

PRX Quantum **3**, 030308 (2022).

[51] <https://github.com/CYI1995/TQS> (2025).

## Appendix A: Supplementary background

### 1. Many-Body Green's Function

In this appendix we give an overview of basic facts about many-body Green's function in condensed matter physics. Suppose  $H$  is a Hamiltonian with a non-degenerate ground state and has eigendecomposition  $H = \sum_{n=0}^{d-1} E_n |n\rangle\langle n|$ . Let  $O_a, O_b$  be two linear operators. The many-body Green's function at zero-temperature is defined as:

$$G(z) := \langle 0 | O_a (z - H + E_0)^{-1} O_b | 0 \rangle = \sum_n \frac{\langle 0 | O_a | n \rangle \langle n | O_b | 0 \rangle}{z - E_n + E_0}, \quad \text{Im}(z) > 0. \quad (\text{A1})$$

Note that for all  $\zeta$  with  $\text{Re}(\zeta) > 0$ , we have  $\int_0^\infty e^{-\zeta t} dt = \zeta^{-1}$ . In conjunction with the fact that

$$C(O_a, O_b, -t) = \sum_n \langle 0 | O_a | n \rangle \langle n | e^{-iHt} O_b e^{iHt} | 0 \rangle = \sum_n \langle 0 | O_a | n \rangle \langle n | O_b | 0 \rangle e^{i(E_0 - E_n)t}, \quad (\text{A2})$$

we obtain

$$\int_0^\infty e^{izt} e^{i(E_0 - E_n)t} dt = \frac{1}{z - E_n + E_0}, \quad \int_0^\infty e^{izt} C(O_a, O_b, -t) dt = G(z). \quad (\text{A3})$$

This confirms Eq. (4) in the main text. Let  $z = \omega + i\eta$  with  $\omega \in \mathbb{R}, \eta \in \mathbb{R}^+$ . Then we have

$$G(z) = G(\omega + i\eta) = \sum_n \langle 0 | O_a | n \rangle \langle n | O_b | 0 \rangle \frac{(\omega - E_n + E_0) - i\eta}{(\omega - E_n + E_0)^2 + \eta^2}. \quad (\text{A4})$$

Let  $\eta > 0$  be a constant, then

$$\begin{aligned} S(\omega, \eta) &:= -2\text{Im}[G(\omega + i\eta)] = \sum_n \langle 0 | O_a | n \rangle \langle n | O_b | 0 \rangle \frac{2\eta}{(\omega - E_n + E_0)^2 + \eta^2}, \\ \int_{-\infty}^\infty \frac{d\omega}{2\pi} \frac{S(\omega, \eta)}{z - \omega} &= \sum_n \langle 0 | O_a | n \rangle \langle n | O_b | 0 \rangle \int_{-\infty}^\infty \frac{d\omega}{2\pi} \frac{2\eta}{(\omega - E_n + E_0)^2 + \eta^2} \frac{1}{z - \omega}. \end{aligned} \quad (\text{A5})$$

Let  $\Delta E_n = E_n - E_0$ , then

$$\begin{aligned} \int_{-\infty}^\infty \frac{d\omega}{2\pi} \frac{2\eta}{(\omega - \Delta E_n)^2 + \eta^2} \frac{1}{z - \omega} &= \int_{-\infty}^\infty \frac{d\omega}{2\pi} \frac{2\eta}{\omega^2 + \eta^2} \frac{1}{z - \omega - \Delta E_n} \\ &= \frac{1}{\pi} \int_{-\infty}^\infty \frac{1}{z - \omega - \Delta E_n} d \arctan(\omega/\eta) \\ &= \frac{1}{\pi} \int_{-\pi/2}^{\pi/2} \frac{1}{z - \eta \tan \theta - \Delta E_n} d\theta \\ &\xrightarrow{\eta \rightarrow 0^+} \frac{1}{z - \Delta E_n}. \end{aligned} \quad (\text{A6})$$

Therefore,

$$\int_{-\infty}^\infty \frac{d\omega'}{2\pi} \frac{S(\omega', 0^+)}{\omega + i0^+ - \omega'} = G(\omega + i0^+) = \sum_n \frac{\langle 0 | O_a | n \rangle \langle n | O_b | 0 \rangle}{\omega - (E_n - E_0)}. \quad (\text{A7})$$

Moreover, we can observe that

$$S(\omega) := \lim_{\eta \rightarrow 0^+} S(\omega, \eta) = 2\pi \sum_n \langle 0 | O_a | n \rangle \langle n | O_b | 0 \rangle \delta(\omega - (E_n - E_0)), \quad (\text{A8})$$

which is termed as the *spectrum function* and it is determined by the imaginary part of  $G(\omega + i0^+)$ .

## 2. Jordan–Wigner Transformation

Jordan–Wigner transformation maps fermionic creation and annihilation operators to Pauli strings on qubits. For a fermionic lattice with  $N$  sites and two spin species, there are  $J = 2N$  spin-orbitals, which we index by  $j \in \{0, 1, \dots, J-1\}$ . The standard Jordan–Wigner mapping is

$$c_j = \left( \prod_{n=0}^{j-1} Z_n \right) \sigma_j^-, \quad \sigma_j^\pm = \frac{X_j \pm iY_j}{2}. \quad (\text{A9})$$

From this mapping one obtains the identities

$$c_j c_j^\dagger = \frac{1 + Z_j}{2}, \quad n_j := c_j^\dagger c_j = \frac{1 - Z_j}{2}, \quad (\text{A10})$$

and, for nearest neighbors,

$$c_j^\dagger c_{j+1} = \sigma_j^+ \sigma_{j+1}^-, \quad c_{j+1}^\dagger c_j = \sigma_{j+1}^+ \sigma_j^-, \quad (\text{A11})$$

which imply the familiar hopping relation

$$c_j^\dagger c_{j+1} + c_{j+1}^\dagger c_j = \frac{X_j X_{j+1} + Y_j Y_{j+1}}{2}. \quad (\text{A12})$$

Finally, note that fermionic bilinears do not commute in general: for example,

$$[c_i^\dagger c_j, c_j^\dagger c_k] = c_i^\dagger c_k \neq 0 \quad (\text{A13})$$

whenever the indices overlap.

## 3. Davies generators and Gibbs-state preparation

We briefly review the Davies generator, a canonical Lindbladian whose fixed point is the Gibbs state. For an arbitrary linear operator  $J$ , define its Heisenberg evolution  $J(t) = e^{iHt} J e^{-iHt}$ . The Bohr-frequency components  $\{J_\nu\}$  are defined by the Fourier decomposition

$$J(t) = \sum_{\nu} J_\nu e^{i\nu t}. \quad (\text{A14})$$

If  $H = \sum_n E_n |\psi_n\rangle\langle\psi_n|$ , then

$$J_\nu = \sum_{m,n: E_m - E_n = \nu} \langle\psi_m|J|\psi_n\rangle |\psi_m\rangle\langle\psi_n|, \quad [H, J_\nu] = \nu J_\nu, \quad J_\nu^\dagger = J_{-\nu}. \quad (\text{A15})$$

Let  $\mathcal{D}(H) = \{E_m - E_n\}$  denote the set of Bohr frequencies. Given rates  $\eta(\nu) \geq 0$ , the Davies generator is

$$\mathcal{L}[\rho] = \sum_{\nu \in \mathcal{D}(H)} \eta(\nu) \left( J_\nu \rho J_\nu^\dagger - \frac{1}{2} \{J_\nu^\dagger J_\nu, \rho\} \right). \quad (\text{A16})$$

Its adjoint (Heisenberg picture) acts as

$$\mathcal{L}^\dagger[O] = \sum_{\nu \in \mathcal{D}(H)} \eta(\nu) \left( J_\nu^\dagger O J_\nu - \frac{1}{2} \{J_\nu^\dagger J_\nu, O\} \right). \quad (\text{A17})$$

**Lemma 1.** *If  $\eta(\nu)e^{\beta\nu} = \eta(-\nu)$  for all  $\nu \in \mathcal{D}(H)$ , then the Davies generator satisfies the Kubo–Martin–Schwinger (KMS) detailed-balance condition:*

$$\mathcal{L}[\cdot] = \rho_\beta^{1/2} \mathcal{L}^\dagger \left[ \rho_\beta^{-1/2} \cdot \rho_\beta^{-1/2} \right] \rho_\beta^{1/2}. \quad (\text{A18})$$

In particular,  $\mathcal{L}[\rho_\beta] = 0$ .

*Proof.* The KMS detailed-balance condition can be expanded as

$$\sum_{\nu} \eta(\nu) \left[ J_{\nu} \cdot J_{\nu}^{\dagger} - \frac{1}{2} \{ J_{\nu}^{\dagger} J_{\nu}, \cdot \} \right] \quad (\text{A19})$$

$$= \sum_{\nu} \eta(\nu) \rho_{\beta}^{-1/2} \left[ J_{\nu}^{\dagger} \rho_{\beta}^{-1/2} \cdot \rho_{\beta}^{-1/2} J_{\nu} - \frac{1}{2} \{ J_{\nu}^{\dagger} J_{\nu}, \rho_{\beta}^{-1/2} \cdot \rho_{\beta}^{-1/2} \} \right] \rho_{\beta}^{-1/2}. \quad (\text{A20})$$

Note that

$$\rho_{\beta}^{1/2} J_{\nu} \rho_{\beta}^{-1/2} = \sum_{(m,n): E_m - E_n = \nu} \langle \psi_m | A | \psi_n \rangle (e^{-\beta E_m/2} e^{\beta E_n/2}) | \psi_m \rangle \langle \psi_n | = e^{-\beta \nu/2} J_{\nu}. \quad (\text{A21})$$

Hence, for all  $\nu \in \mathcal{D}(H)$ , we have

$$\eta(\nu) \rho_{\beta}^{1/2} J_{\nu}^{\dagger} \rho_{\beta}^{-1/2} \cdot \rho_{\beta}^{-1/2} J_{\nu} \rho_{\beta}^{1/2} = \eta(\nu) e^{\beta \nu} A_{-\nu} \cdot A_{-\nu}^{\dagger} = \eta(-\nu) A_{-\nu} \cdot A_{-\nu}^{\dagger}. \quad (\text{A22})$$

That is,

$$\sum_{\nu} \eta(\nu) \rho_{\beta}^{1/2} J_{\nu}^{\dagger} \rho_{\beta}^{-1/2} \cdot \rho_{\beta}^{-1/2} J_{\nu} \rho_{\beta}^{1/2} = \sum_{\nu} \eta(-\nu) A_{-\nu} \cdot A_{-\nu}^{\dagger} = \sum_{\nu} \eta(\nu) J_{\nu} \cdot J_{\nu}^{\dagger}. \quad (\text{A23})$$

Because  $[H, J_{\nu}^{\dagger} J_{\nu}] = 0$ , we further have  $[\rho_{\beta}^{\pm 1/2}, J_{\nu}^{\dagger} J_{\nu}] = 0$ , and

$$\rho_{\beta}^{1/2} \left\{ J_{\nu}^{\dagger} J_{\nu}, \rho_{\beta}^{-1/2} \cdot \rho_{\beta}^{-1/2} \right\} \rho_{\beta}^{1/2} = \{ J_{\nu}^{\dagger} J_{\nu}, \cdot \}. \quad (\text{A24})$$

In particular, we have

$$\mathcal{L}[\rho_{\beta}] = \rho_{\beta}^{1/2} \mathcal{L}^{\dagger}[I] \rho_{\beta}^{1/2} = \rho_{\beta}, \quad (\text{A25})$$

which implies that  $\mathcal{L}[\rho_{\beta}] = 0$ . □

## Appendix B: Proof of Main Results

### 1. Proof of Lemma 1

*Proof.* Observe that

$$\langle n | A | m \rangle = -\langle n | P A P | m \rangle = -p_m p_n \langle n | A | m \rangle. \quad (\text{B1})$$

Hence, if  $p_n p_m = 1$ , then  $\langle n | A | m \rangle = 0$ . Conversely, if  $\langle n | A | m \rangle \neq 0$ , then  $p_n p_m = -1$ . This completes the proof of Lemma 1. □

### 2. Proof of Theorem 1

**Lemma 2.** *Suppose  $\rho$  commutes with  $P$ , and observables  $O_1, \dots, O_L$  all anti-commute with  $P$ . If  $L$  is odd, then*

$$\text{Tr} \left( \rho \prod_{\ell=1}^L O_{\ell} \right) = 0. \quad (\text{B2})$$

*Proof.* Note that

$$P \prod_{\ell=1}^L O_{\ell} = - \prod_{\ell=1}^L O_{\ell} P. \quad (\text{B3})$$

Hence,

$$\text{Tr} \left( \rho \prod_{\ell=1}^L O_{\ell} \right) = \text{Tr} \left( P \rho P \prod_{\ell=1}^L O_{\ell} \right) = - \text{Tr} \left( \rho \prod_{\ell=1}^L O_{\ell} P^2 \right) = - \text{Tr} \left( \rho \prod_{\ell=1}^L O_{\ell} \right). \quad (\text{B4})$$

□

With the above observation, we present the proof of Theorem 1 as follows.

*Proof.* By definition, we have

$$Q_{\rho,B}(e^{-iHt}A) = \text{Tr}(e^{-iHt}A\rho A e^{iHt}B) = \text{Tr}(\rho AB(t)A). \quad (\text{B5})$$

Since  $\{A, P\} = \{B(t), P\} = [\rho, P] = 0$ , in conjunction with Lemma 2, we have  $Q_{\rho,B}(e^{-iHt}A) = 0$ . Similarly, we have  $Q_{\rho,B}(e^{-iHt}) = Q_{\rho,B}(e^{-iHt}P) = 0$ . This confirms that

$$\begin{aligned} Q_{\rho,B}(e^{-iHt}U_{\text{Im}}) &= \text{Tr}\left[e^{-iHt}\frac{I+iA}{\sqrt{2}}\rho\frac{I-iA}{\sqrt{2}}e^{iHt}B\right] \\ &= \text{Im}[C(A, B, t)] + \frac{1}{2}Q_{\rho,B}(e^{-iHt}) + \frac{1}{2}Q_{\rho,B}(e^{-iHt}A) \\ &= \text{Im}[C(A, B, t)], \end{aligned} \quad (\text{B6})$$

$$\begin{aligned} Q_{\rho,B}(e^{-iHt}U_{\text{Re}}) &= \text{Tr}\left[e^{-iHt}\frac{P+A}{\sqrt{2}}\rho\frac{P+A}{\sqrt{2}}e^{iHt}B\right] \\ &= \text{Re}[C(PA, B, t)] + \frac{1}{2}Q_{\rho,B}(e^{-iHt}P) + \frac{1}{2}Q_{\rho,B}(e^{-iHt}A) \\ &= \text{Re}[C(PA, B, t)]. \end{aligned} \quad (\text{B7})$$

Because  $\rho P = p\rho$  with  $p \in \{\pm 1\}$ , we further have

$$C(PA, B, t) = \text{Tr}(\rho PAB(t)) = p \text{Tr}(\rho AB(t)) = pC(A, B, t). \quad (\text{B8})$$

This completes the proof of Theorem 1.  $\square$

### 3. Proof of Theorem 2

*Proof.* Recall the decomposition

$$\rho_\beta = \frac{1 + \text{Tr}(\rho_\beta P)}{2} \rho_S + \frac{1 - \text{Tr}(\rho_\beta P)}{2} \rho_A, \quad (\text{B9})$$

where  $P\rho_S = \rho_S$  and  $P\rho_A = -\rho_A$ . By linearity of the correlator in the state, we have

$$C(A, B, t) = \text{Tr}(\rho_\beta AB(t)) = \frac{1 + \text{Tr}(\rho_\beta P)}{2} \text{Tr}(\rho_S AB(t)) + \frac{1 - \text{Tr}(\rho_\beta P)}{2} \text{Tr}(\rho_A AB(t)). \quad (\text{B10})$$

Taking real parts yields

$$\text{Re}[C(A, B, t)] = \frac{1 + \text{Tr}(\rho_\beta P)}{2} \text{Re}[\text{Tr}(\rho_S AB(t))] + \frac{1 - \text{Tr}(\rho_\beta P)}{2} \text{Re}[\text{Tr}(\rho_A AB(t))]. \quad (\text{B11})$$

Now apply Theorem 1 to each parity sector. Since  $\rho_S$  has definite parity  $p = +1$  and  $\rho_A$  has definite parity  $p = -1$ , we obtain

$$\text{Re}[\text{Tr}(\rho_S AB(t))] = Q_{\rho_S, B}(e^{-iHt}U_{\text{Re}}), \quad \text{Re}[\text{Tr}(\rho_A AB(t))] = -Q_{\rho_A, B}(e^{-iHt}U_{\text{Re}}). \quad (\text{B12})$$

Substituting into the previous expression gives Eq. (29), completing the proof.  $\square$

### Appendix C: Signal analysis algorithm

We use the Multiple Signal Classification (MUSIC) algorithm [45] to estimate the frequencies appearing in the time-domain correlator. Consider a length- $(2N)$  time-domain signal of the form

$$s_n = \sum_{k=1}^X c_k e^{-if_k n}, \quad f_k \in [0, 2\pi], \quad n = 0, 1, \dots, 2N-1, \quad (\text{C1})$$

where  $\chi$  is the number of spectral lines (model order). Construct the Hankel matrix  $M \in \mathbb{C}^{N \times N}$  by

$$M_{m,n} := s_{m+n}, \quad m, n = 0, 1, \dots, N-1. \quad (\text{C2})$$

If  $N \geq \chi$ , then in the noiseless setting  $\text{rank}(M) \leq \chi$ .

Let  $M = U\Sigma V^\dagger$  be the singular value decomposition, with singular values in non-increasing order. Write

$$U = [U_{\text{sig}} \ U_{\text{noise}}], \quad (\text{C3})$$

where  $U_{\text{sig}} \in \mathbb{C}^{N \times \chi}$  contains the first  $\chi$  left singular vectors (signal subspace) and  $U_{\text{noise}} \in \mathbb{C}^{N \times (N-\chi)}$  contains the remaining vectors (noise subspace). Define the steering vector

$$a(\omega) := [e^{-i\omega n}]_{n=0}^{N-1}. \quad (\text{C4})$$

Then  $a(f_k)$  lies in the signal subspace, equivalently it is orthogonal to the noise subspace:

$$U_{\text{noise}}^\dagger a(f_k) = 0, \quad k = 1, \dots, \chi. \quad (\text{C5})$$

This motivates the MUSIC noise-subspace correlation function

$$R(\omega) := \|U_{\text{noise}}^\dagger a(\omega)\|_2, \quad (\text{C6})$$

whose local minimas occur near the true frequencies  $\{f_k\}_{k=1}^\chi$ .

We recall an established stability result for MUSIC under additive i.i.d. noise.

**Theorem 1** (Corollary 1 in [45]). *Suppose  $(s_n)_{n=0}^{2N-1}$  is a length- $(2N)$  signal of the form Eq. (C1) satisfying the minimum separation condition*

$$\min_{k_1 \neq k_2} |f_{k_1} - f_{k_2}| = \Omega(N^{-1}). \quad (\text{C7})$$

Let  $(e_n)_{n=0}^{2N-1}$  be i.i.d. random variables with variance  $\sigma^2$ , and run MUSIC on the noisy samples  $(s_n + e_n)_{n=0}^{2N-1}$ , producing  $\tilde{R}(\omega)$ . Then with high probability,

$$\max_{\omega} |\tilde{R}(\omega) - R(\omega)| = \mathcal{O}(\sigma N^{-1/2}). \quad (\text{C8})$$

Unfortunately, the bound Eq. (C8) does not directly translate into an explicit estimation error for the frequencies  $f_k$ . In favorable regimes, the achievable frequency error can be as small as  $\mathcal{O}(\sigma N^{-3/2})$ ; see, e.g., Remark 11 of [45].

---

### Algorithm 2 MUSIC (basic form)

---

**Input:** Signal  $(s_n)_{n=1}^{2N}$ ; model order  $\chi$

**Output:** Frequency estimates  $\{\hat{f}_k\}_{k=1}^\chi$ .

- 1: Form  $M \in \mathbb{C}^{N \times N}$  with  $M_{m,n} = s_{m+n}$  for  $m, n = 0, \dots, N-1$
  - 2: Compute an SVD  $M = U\Sigma V^*$
  - 3: Let  $U_{\text{noise}} := [u_{\chi+1}, \dots, u_N]$  (columns spanning the noise subspace)
  - 4: For a frequency grid  $\omega \in [0, 2\pi]$ , evaluate  $R(\omega) = \|U_{\text{noise}}^\dagger a(\omega)\|_2$ .
  - 5: Return the  $\chi$  dominant local minimas of  $R(\omega)$  as  $\{\hat{f}_k\}$ .
- 

### Appendix D: Computing time correlators via mid-circuit measurements

In this section, we summarize a slightly simplified mid-circuit measurement (MCM) protocol (adapted from [30]) for estimating two-point correlators for general initial states. We include it here for its simplicity and generality. However, unlike our TQS protocol (which uses only end-of-circuit measurements), MCM-based estimators can be particularly sensitive to mid-circuit measurement imperfections such as readout-induced dephasing, crosstalk, and imperfect reset.

Let  $A$  and  $B$  be Pauli observables with eigenvalues  $\pm 1$ . Measuring  $A$  corresponds to the projective measurement  $\{\Pi_+^A, \Pi_-^A\}$  with

$$\Pi_{\pm}^A = \frac{I \pm A}{2}. \quad (\text{D1})$$

For an initial state  $\rho$ , the outcome  $o_1 \in \{+1, -1\}$  occurs with probability

$$\Pr(o_1) = \text{Tr}(\rho \Pi_{o_1}^A), \quad (\text{D2})$$

and the post-measurement state is

$$\rho_{o_1} = \frac{\Pi_{o_1}^A \rho \Pi_{o_1}^A}{\Pr(o_1)}. \quad (\text{D3})$$

Conditioned on  $o_1$ , we next measure  $B$  using  $\Pi_{\pm}^B = (I \pm B)/2$ , obtaining  $o_2 \in \{\pm 1\}$ . The joint probability is

$$\Pr(o_1, o_2) = \text{Tr}(\Pi_{o_2}^B \Pi_{o_1}^A \rho \Pi_{o_1}^A). \quad (\text{D4})$$

A direct calculation shows that

$$\mathbb{E}[o_1 o_2] = \sum_{o_1, o_2 \in \{\pm 1\}} o_1 o_2 \Pr(o_1, o_2) = \frac{1}{2} \text{Tr}(\rho(AB + BA)) = \text{Re}[\text{Tr}(\rho AB)]. \quad (\text{D5})$$

Therefore,  $\text{Re}[\text{Tr}(\rho AB)]$  can be estimated by repeating the two-step measurement and averaging the product  $o_1 o_2$  over many shots.